

# Search for Majorana neutrinos with the first two years of EXO-200 data

J.B. Albert,<sup>1</sup> D.J. Auty,<sup>2</sup> P.S. Barbeau,<sup>3</sup> E. Beauchamp,<sup>4</sup> D. Beck,<sup>5</sup> V. Belov,<sup>6</sup> C. Benitez-Medina,<sup>7</sup> J. Bonatt,<sup>8,9</sup> M. Breidenbach,<sup>10</sup> T. Brunner,<sup>9</sup> A. Burenkov,<sup>6</sup> G.F. Cao,<sup>11</sup> C. Chambers,<sup>7</sup> J. Chaves,<sup>9</sup> B. Cleveland,<sup>4, a</sup> M. Coon,<sup>5</sup> A. Craycraft,<sup>7</sup> T. Daniels,<sup>8</sup> M. Danilov,<sup>6</sup> S.J. Daugherty,<sup>1</sup> C.G. Davis,<sup>12</sup> J. Davis,<sup>9</sup> R. DeVoe,<sup>9</sup> S. Delaquis,<sup>13</sup> T. Didberidze,<sup>2</sup> A. Dolgolenko,<sup>6</sup> M.J. Dolinski,<sup>14</sup> M. Dunford,<sup>15</sup> W. Fairbank Jr.,<sup>7</sup> J. Farine,<sup>4</sup> W. Feldmeier,<sup>16</sup> P. Fierlinger,<sup>16</sup> D. Fudenberg,<sup>9</sup> G. Giroux,<sup>13, b</sup> R. Gornea,<sup>13</sup> K. Graham,<sup>15</sup> G. Gratta,<sup>9</sup> C. Hall,<sup>12</sup> S. Herrin,<sup>10</sup> M. Hughes,<sup>2</sup> M.J. Jewell,<sup>14</sup> X.S. Jiang,<sup>11</sup> A. Johnson,<sup>10</sup> T.N. Johnson,<sup>1</sup> S. Johnston,<sup>8</sup> A. Karelin,<sup>6</sup> L.J. Kaufman,<sup>1</sup> R. Killick,<sup>15</sup> T. Koffas,<sup>15</sup> S. Kravitz,<sup>9</sup> A. Kuchenkov,<sup>6</sup> K.S. Kumar,<sup>8</sup> D.S. Leonard,<sup>17</sup> F. Leonard,<sup>15</sup> C. Licciardi,<sup>15</sup> Y.H. Lin,<sup>14</sup> R. MacLellan,<sup>10</sup> M.G. Marino,<sup>16, c</sup> B. Mong,<sup>4</sup> D. Moore,<sup>9</sup> R. Nelson,<sup>18</sup> A. Odian,<sup>10</sup> I. Ostrovskiy,<sup>9</sup> C. Ouellet,<sup>15</sup> A. Piepke,<sup>2</sup> A. Pocar,<sup>8</sup> C.Y. Prescott,<sup>10</sup> A. Rivas,<sup>9</sup> P.C. Rowson,<sup>10</sup> M.P. Roza,<sup>15</sup> J.J. Russell,<sup>10</sup> A. Schubert,<sup>9</sup> D. Sinclair,<sup>15, 19</sup> S. Slutsky,<sup>12</sup> E. Smith,<sup>14</sup> V. Stekhanov,<sup>6</sup> M. Tarka,<sup>5</sup> T. Tolba,<sup>13</sup> D. Tosi,<sup>9, d</sup> K. Twelker,<sup>9</sup> P. Vogel,<sup>20</sup> J.-L. Vuilleumier,<sup>13</sup> A. Waite,<sup>10</sup> J. Walton,<sup>5</sup> T. Walton,<sup>7</sup> M. Weber,<sup>9</sup> L.J. Wen,<sup>11</sup> U. Wichoski,<sup>4</sup> J.D. Wright,<sup>8</sup> L. Yang,<sup>5</sup> Y.-R. Yen,<sup>12</sup> O.Ya. Zeldovich,<sup>6</sup> and Y.B. Zhao<sup>11</sup>

(EXO-200 Collaboration)

<sup>1</sup>*Physics Department and CEEM, Indiana University, Bloomington IN, USA*

<sup>2</sup>*Department of Physics and Astronomy, University of Alabama, Tuscaloosa AL, USA*

<sup>3</sup>*Department of Physics, Duke University, and Triangle Universities Nuclear Laboratory (TUNL), Durham, North Carolina, USA*

<sup>4</sup>*Department of Physics, Laurentian University, Sudbury ON, Canada*

<sup>5</sup>*Physics Department, University of Illinois, Urbana-Champaign IL, USA*

<sup>6</sup>*Institute for Theoretical and Experimental Physics, Moscow, Russia*

<sup>7</sup>*Physics Department, Colorado State University, Fort Collins CO, USA*

<sup>8</sup>*Physics Department, University of Massachusetts, Amherst MA, USA*

<sup>9</sup>*Physics Department, Stanford University, Stanford CA, USA*

<sup>10</sup>*SLAC National Accelerator Laboratory, Stanford CA, USA*

<sup>11</sup>*Institute of High Energy Physics, Beijing, China*

<sup>12</sup>*Physics Department, University of Maryland, College Park MD, USA*

<sup>13</sup>*LHEP, Albert Einstein Center, University of Bern, Bern, Switzerland*

<sup>14</sup>*Department of Physics, Drexel University, Philadelphia PA, USA*

<sup>15</sup>*Physics Department, Carleton University, Ottawa ON, Canada*

<sup>16</sup>*Technische Universität München, Physikdepartment and Excellence Cluster Universe, Garching, Germany*

<sup>17</sup>*Department of Physics, University of Seoul, Seoul, Korea*

<sup>18</sup>*Waste Isolation Pilot Plant, Carlsbad NM, USA*

<sup>19</sup>*TRIUMF, Vancouver, BC, Canada*

<sup>20</sup>*Kellogg Lab, Caltech, Pasadena, CA, USA*

(Dated: February 28, 2014)

We report on new results from the EXO-200 double-beta-decay experiment with 99.8 kg-yr of <sup>136</sup>Xe exposure, representing an almost fourfold increase from earlier publications. The detector resolution at the <sup>136</sup>Xe double-beta-decay Q-value has been improved to  $\sigma/E = 1.53\%$  and the background in the  $\pm 2\sigma$  region of interest has been determined to be  $(1.7 \pm 0.2) \cdot 10^{-3} \text{ keV}^{-1} \text{ kg}^{-1} \text{ yr}^{-1}$ , consistent with previous results. Both the exposure and the background rate are among the best in the literature, resulting in a 90% CL half-life sensitivity of  $1.9 \cdot 10^{25} \text{ yr}$ . We find no statistically significant evidence for  $0\nu\beta\beta$  decay and set a half-life limit of  $1.1 \cdot 10^{25} \text{ yr}$  at 90% CL.

PACS numbers: 23.40.-s, 21.10.Tg, 14.60.Pq, 27.60.+j

Majorana fermions, neutral spin-1/2 particles described by 2-component spinors, have been an element of quantum field theory since its inception [1, 2]. Electrons and other spin-1/2 elementary particles with distinct antiparticles, however, are described by 4-component Dirac

spinors. Majorana quasiparticles may have been observed in condensed matter systems [3] where neutrality is achieved through the collective action of electrons and holes. Among the known *elementary* particles, only neutrinos are Majorana fermion candidates, owing to their intrinsic neutrality. Confirmation of this property would imply the non-conservation of lepton number, an additive quantum number that, unlike charge or color, is not related to any known gauge symmetry. As yet, lepton number has been empirically found to be conserved. Neutrinos are also remarkable for their small, yet finite,

<sup>a</sup> Also SNOLAB, Sudbury ON, Canada

<sup>b</sup> Now at Queen's University, Kingston, ON, Canada

<sup>c</sup> Corresponding author: michael.marino@mytum.de

<sup>d</sup> Now at University of Wisconsin, Madison, WI, USA

masses [4] that are generally difficult to explain, but arise naturally in many extensions [5, 6] of the Standard Model of particle physics (SM). A generic consequence of many such extensions is that neutrinos should be of the Majorana variety.

The most sensitive probe for Majorana neutrinos is a nuclear process known as neutrinoless double-beta decay ( $0\nu\beta\beta$ ), whereby a nucleus decays by emitting two electrons and nothing else, while changing its charge by two units [7]. A related double-beta decay process, known as two-neutrino double-beta decay ( $2\nu\beta\beta$ ), is allowed by the SM and has been observed in many nuclei,  $^{136}\text{Xe}$  among them [8, 9]. It provides, however, no direct information on the Majorana/Dirac question. The exotic  $0\nu\beta\beta$  can be distinguished from the  $2\nu\beta\beta$  by measuring the sum energy of the two electrons that is peaked at the Q-value for the former and is a continuum for the latter. We refer to this region around the Q-value as the  $0\nu\beta\beta$  region-of-interest (ROI). The half-life of the  $0\nu\beta\beta$  is related to the effective Majorana neutrino mass ( $\langle m_{\beta\beta} \rangle$ ) by a phase space factor and a nuclear matrix element. Hence the observation of the  $0\nu\beta\beta$  decay would discover elementary Majorana particles, demonstrate lepton number violation and measure the neutrino mass scale  $\langle m_{\beta\beta} \rangle$ , at least to within the theoretical uncertainty of the nuclear matrix elements [10].

Recent sensitive searches for  $0\nu\beta\beta$  have been carried out in  $^{76}\text{Ge}$  (GERDA [11]) and  $^{136}\text{Xe}$  (KamLAND-Zen [12] and EXO-200 [13]). These experiments have set limits on the Majorana neutrino mass of  $\sim 0.2\text{--}0.3$  eV, and have cast doubt on an earlier claim of observation [14]. In this letter we report on new  $0\nu\beta\beta$  search results from the EXO-200 experiment based upon about two years of data.

EXO-200 has been described in detail elsewhere [15]. Briefly, the detector is a cylindrical liquid xenon (LXe) time projection chamber (TPC), roughly 40 cm in diameter and 44 cm in length. Two drift regions are separated in the center by a cathode. The LXe is enriched to 80.6% in  $^{136}\text{Xe}$ , the  $0\nu\beta\beta$  candidate ( $Q = 2457.83 \pm 0.37$  keV [16]). The TPC provides X-Y-Z coordinate and energy measurements of ionization deposits in the LXe by simultaneously collecting the scintillation light and the charge. Charge deposits spatially separated by about 1 cm or more are individually observed and the position accuracy for isolated deposits is a few mm. Avalanche Photodiodes (APDs) measure the scintillation light. Small radioactive sources can be positioned at standard positions near the TPC to calibrate the detector and monitor its stability.

The TPC is shielded from environmental radioactivity on all sides by  $\sim 50$  cm of HFE-7000 cryofluid [17] (HFE) maintained at  $\sim 167$  K inside a vacuum-insulated copper cryostat. Further shielding is provided by at least 25 cm of lead in all directions. The entire assembly is housed underground in a cleanroom at a depth of  $1585^{+11}_{-6}$  meters water equivalent [18] at the Waste Isolation Pilot Plant near Carlsbad, NM, USA. Four of the six sides of

the cleanroom are instrumented with plastic scintillator panels recording the passage of cosmic ray muons. An extensive materials screening campaign [19] was employed to minimize the radioactive background produced by the detector components.

The data analysis methods in this work follow closely those presented in detail in [9]. Events in the detector are classified as single-site (SS) or multi-site (MS) according to the number of detected charge deposits.  $0\nu\beta\beta$  events are predominantly SS whereas  $\gamma$  backgrounds are mostly MS. For each event, the energy is determined as a linear combination of charge and scintillation, while a “standoff distance” (SD) is defined as the distance between a charge deposit and the closest material that is not LXe, other than the cathode. To search for  $0\nu\beta\beta$ , a binned maximum-likelihood (ML) fit is performed simultaneously over the SS and MS events using probability density functions (PDFs) in energy and SD, generated using a Geant4-based [20] Monte Carlo simulation (MC). The energy range 980–9800 keV is used. The ‘low-background data set’ (physics data) is obtained after applying event selection cuts. With respect to Ref. [9] the current analysis additionally includes: (1) improved signal processing for the scintillation waveforms resulting in lower noise; (2)  $^{226}\text{Ra}$  source calibration data; (3) an expanded fiducial volume; (4) the estimation of systematic errors related to the  $0\nu\beta\beta$  ROI; and (5) updated background and systematic studies relevant to the  $0\nu\beta\beta$  search.

The data set presented here (Run 2) combines Run 2a (already used for [9, 13], September 22, 2011 – April 15, 2012) and Runs 2b and 2c (April 16, 2012 – September 1, 2013). After removing periods of poor data quality and calibration runs, the total amount of low-background data for this analysis is  $477.60 \pm 0.01$  days, a 3.8-fold increase from previous EXO-200 publications. The primary tool used for understanding and correcting the detector energy measurement is the 2615 keV  $\gamma$  line of  $^{208}\text{Tl}$  from a  $^{228}\text{Th}$  source deployed at least twice weekly during the time spanned by this data set. Seven multi-day calibration campaigns involving the use of multiple sources ( $^{228}\text{Th}$ ,  $^{60}\text{Co}$ ,  $^{226}\text{Ra}$  and  $^{137}\text{Cs}$ ) were performed at roughly 3-month intervals throughout the data set. The lifetime of ionization electrons in the LXe is better than 2 ms for the entire data set, more than sufficient to collect charge across the full volume of the detector. We determine the optimal linear combination of scintillation and ionization signals once per week by minimizing the width of the 2615 keV line. To prevent making analysis decisions that could bias the results in the ROI, the low-background data were partially “masked” to hide  $\sim 2/3$  of the live-time for SS events between 2325 and 2550 keV. Live-time already analyzed in previous publications (e.g. Run 2a) was not masked.

The energy resolution of the detector is dominated by electronic noise in the scintillation readout and exhibits variations over time due to changes in this noise. We apply a denoising algorithm to the scintillation signals

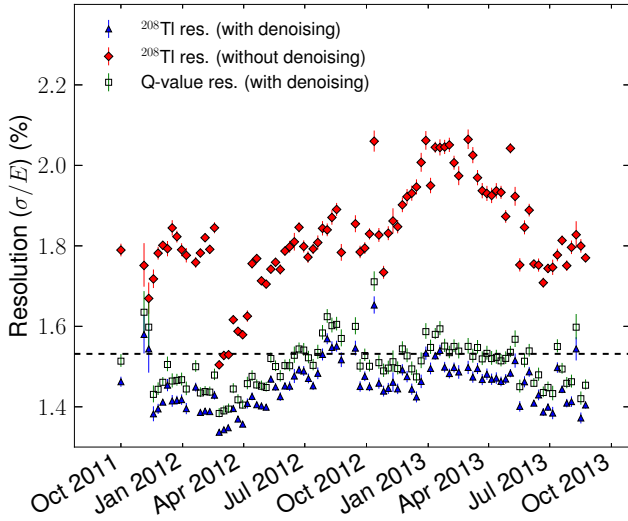


FIG. 1. (Color online) Resolution ( $\sigma/E$ ) for SS events versus time with and without application of the denoising algorithm. Shown are resolutions at the 2615 keV  $^{208}\text{Tl}$  full-absorption peak (with and without) and at the  $0\nu\beta\beta$  Q-value (with). The time variation is caused by changes in the noise of the APD front-end electronics. The horizontal dashed line shows the effective Q-value SS energy resolution used for the data set (1.53%). MS resolution (not shown) exhibits similar behavior.

during post processing, improving the detector resolution and reducing its time dependence. Figure 1 shows the resolution with and without denoising.

We define an effective, time-independent energy resolution function [9]  $\sigma^2(E) = \sigma_{\text{elec}}^2 + b^2E + c^2E^2$ .  $\sigma_{\text{elec}}$ ,  $b$  and  $c$  are 20.8 keV, 0.628 keV $^{1/2}$  and  $1.10 \cdot 10^{-3}$  (25.8 keV, 0.602 keV $^{1/2}$  and  $4.04 \cdot 10^{-3}$ ) for SS (MS), determined by a ML fit to calibration data taken during Run 2. This function is folded with the energy distributions derived from the simulation to create the PDFs used in final fits. The effective resolution ( $\sigma/E$ ) for SS (MS) at the  $0\nu\beta\beta$  Q-value is  $1.53 \pm 0.06\%$  ( $1.65 \pm 0.05\%$ ).

The fiducial volume (FV) is larger than in [9] to maximize the sensitive mass while maintaining systematic uncertainties at an acceptable level. Events in the FV are required to have  $182 \text{ mm} > |Z| > 10 \text{ mm}$  (where  $Z = 0$  is the cathode plane) and are contained in a hexagon with 162 mm apothem. This represents a  $^{136}\text{Xe}$  mass of 76.3 kg, corresponding to  $3.39 \times 10^{26}$  atoms of  $^{136}\text{Xe}$  and, with the quoted live-time, results in an exposure of 99.8 kg·yr (736 mol·yr).

The main systematic uncertainties relevant to the search for  $0\nu\beta\beta$  are related to (1) signal efficiency, (2) location of the  $0\nu\beta\beta$  ROI within the spectrum, and (3) estimation of the background in the ROI.

To verify the simulation's ability to model efficiencies and the background, we compare measurement and simulation of calibration sources deployed at various positions around the TPC, investigating in particular: (a) the energy and SD distributions, (b) the integrated rate of se-

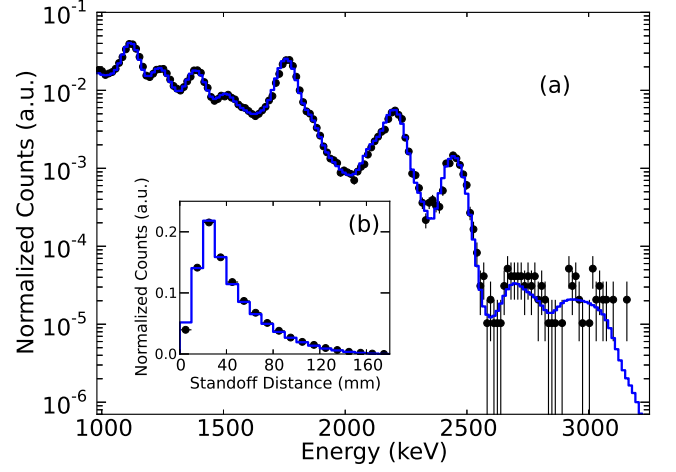


FIG. 2. (Color online) Shape comparison between data (black points) and simulation (blue line) for a  $^{226}\text{Ra}$  calibration source near the cathode outside the TPC, showing energy (a) and SD (b) for SS events.

lected events, and (c) the SS/MS event ratio versus energy. A representative set of results for (a) is shown in Fig. 2, where simulation-data agreement for the  $^{226}\text{Ra}$  source are presented.  $^{226}\text{Ra}$  is a particularly valuable source because of several  $\gamma$  lines that map a broad energy region including the  $0\nu\beta\beta$  ROI. The energy spectrum shows good agreement across the energy range of the analysis. Comparable results were also obtained with the  $^{60}\text{Co}$  and  $^{228}\text{Th}$  sources. The SD agreement is within statistical errors except in the first 10 mm bin, where the simulation produces more events in the FV than seen in data.

Discrepancies in the shapes of energy and SD distributions between data and simulation affect the estimation of the background in the  $0\nu\beta\beta$  ROI. To quantify this effect, we calculate skewing functions based upon the small discrepancies observed in source calibration studies. We distort the background PDFs with the skewing functions and use these to produce a set of toy MC data sets. The toy MC data sets are then fit to un-skewed PDFs. The change in the  $0\nu\beta\beta$  ROI background is 9.2%, which we take as systematic error.

In the rate comparison studies (b), we combine the total number of selected events in data and simulation as  $(\text{Data} - \text{MC})/\text{Data}$  for several source positions. The error-weighted average of the results is calculated using the FV in this analysis as well as the FV in [9]. The difference between these values is 1.7%, which we combine with the underlying FV uncertainty (1.7%, [9]) conservatively assuming full correlation to produce a total error on the detector efficiency of 3.4%.

The ratio of the number of SS events to the total number of events ( $\text{SS}/(\text{SS}+\text{MS})$ ) is compared between data and simulation for 3 sources in Fig. 3. The general behavior is largely independent of the underlying spectral shape. We choose to assign a single systematic

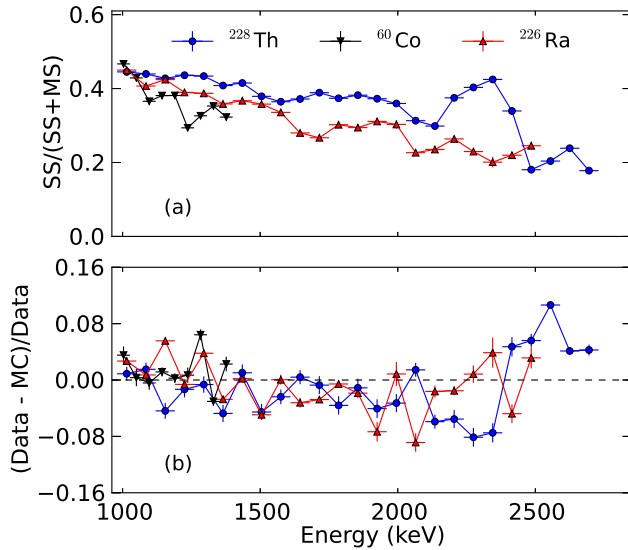


FIG. 3. (Color online) (a) SS/(SS+MS) ratio in data for  $^{226}\text{Ra}$ ,  $^{60}\text{Co}$  and  $^{228}\text{Th}$  calibration sources. (b) Comparison of SS/(SS+MS) ratio between data and simulation for the three sources. Despite having different underlying energy spectra, all sources exhibit similar behavior across the shown energy range when comparing data and simulation (b).

uncertainty to the SS/(SS+MS) ratio of 9.6%, calculated from the weighted average of the maximum deviations observed for the  $^{228}\text{Th}$ ,  $^{60}\text{Co}$  and  $^{226}\text{Ra}$  (data from the latter available after June 2013) sources in each calibration campaign.

Event selection requires an event to be fully reconstructed in all 3 coordinates (X, Y and Z). We compare the relative efficiency of this requirement for  $2\nu\beta\beta$  from MC to the measured relative efficiency derived from the background-subtracted low-background energy spectrum. The relative efficiency from simulation changes modestly across the  $2\nu\beta\beta$  energy range ( $> 99\%$  to  $90\%$  from 980 keV to 2450 keV) and similar behavior is seen in data. The average deviation between simulation and data over the  $2\nu\beta\beta$  spectrum (7.8%) is taken as a systematic error on the efficiency.

The uncertainty on the location of the ROI in the spectrum is dominated by a possible energy-scale difference between  $\beta$ -like events in the LXe (e.g.  $0\nu\beta\beta$ ) and  $\gamma$ -like events (including most backgrounds and the sources used for the primary energy calibration). We define the ‘ $\beta$ -scale’ as  $E_\beta = BE_\gamma$ , where  $E_\beta$  ( $E_\gamma$ ) is the energy for depositions from  $\beta$ s ( $\gamma$ s) and  $B$  is a measured constant. We determine the  $\beta$ -scale by fitting to the  $2\nu\beta\beta$ -decay-dominated low-background data and find  $B = 0.999 \pm 0.002$ .

Several cross checks were performed to search for energy dependence in the  $\beta$ -scale. The above fits were performed using different energy thresholds and with different background PDFs produced using the skewing functions discussed earlier. We also fit the low-background

Source	Signal eff. (%)	Error (%)
Event selections		
Summary from [9]	93.1	0.9
Partial reconstruction	90.9	7.8
Fiducial Volume/Rate agreement	-	3.4
Total	84.6	8.6

TABLE I.  $0\nu\beta\beta$  signal efficiency in the fiducial volume and associated systematic errors from various sources. ‘Partial reconstruction’ refers to the requirement that all events be fully reconstructed in X,Y and Z. The summary for event selection from [9] includes all efficiencies and related errors except fiducial volume and partial reconstruction, which have been recalculated in this work for  $0\nu\beta\beta$ .

data assuming a linear energy dependence (e.g.  $p_0 + p_1 E_\gamma$ ) for  $B$ . In all cases the results are consistent with the original fit, providing no evidence for energy dependence of the  $\beta$ -scale. The estimate of the  $\beta$ -scale is also robust against a different choice of  $2\nu\beta\beta$  spectral shape [21].

To investigate the dependence of the ROI background estimate on the completeness of the fit model, we derive PDFs from different source locations and introduce them separately into the default background model used in the fit. The relative change of the estimated ROI background is then determined. The three background PDFs considered in this study are  $^{238}\text{U}$  in the HFE and inner cryostat, and  $^{60}\text{Co}$  in the copper source guide tube. These were chosen because the initial source location affects relative amplitudes and spectral features in the ROI, i.e. the  $^{214}\text{Bi}$   $\gamma$  (2448 keV) and  $^{60}\text{Co}$  sum peak. This study indicates a total possible deviation of 5.7% for the expected background counts in the ROI.

The residual time dependence of the energy resolution (Fig. 1) can introduce additional counts in the ROI from the 2615 keV  $^{208}\text{Tl}$  peak. This was estimated to affect the ROI background counts by  $\pm 1.5\%$ .

A summary of the  $0\nu\beta\beta$  signal efficiency and associated uncertainty is presented in Table I. Table II summarizes the uncertainties on the estimation of background in the ROI. These errors are explicitly included as input to the final fit to the low-background data. Items not listed in the tables, such as the  $\beta$ -scale and the SS/MS ratios, still contribute to the total systematic error on the  $0\nu\beta\beta$  signal as they are propagated to the final result by the ML fit to the low-background data.

Neutrons arising from cosmic-ray muons or radioactive decays in the salt surrounding the laboratory may contribute background to the  $0\nu\beta\beta$  ROI via neutron capture or spallation processes. The contribution in the ROI is expected to arise primarily from neutron-capture  $\gamma$ s in the LXe and surrounding materials (e.g. capture on  $^{63}\text{Cu}$  and  $^{65}\text{Cu}$  in the copper components, and on  $^{136}\text{Xe}$  in the LXe). A simulation using a simplified experimental geometry and employing the FLUKA [22] and

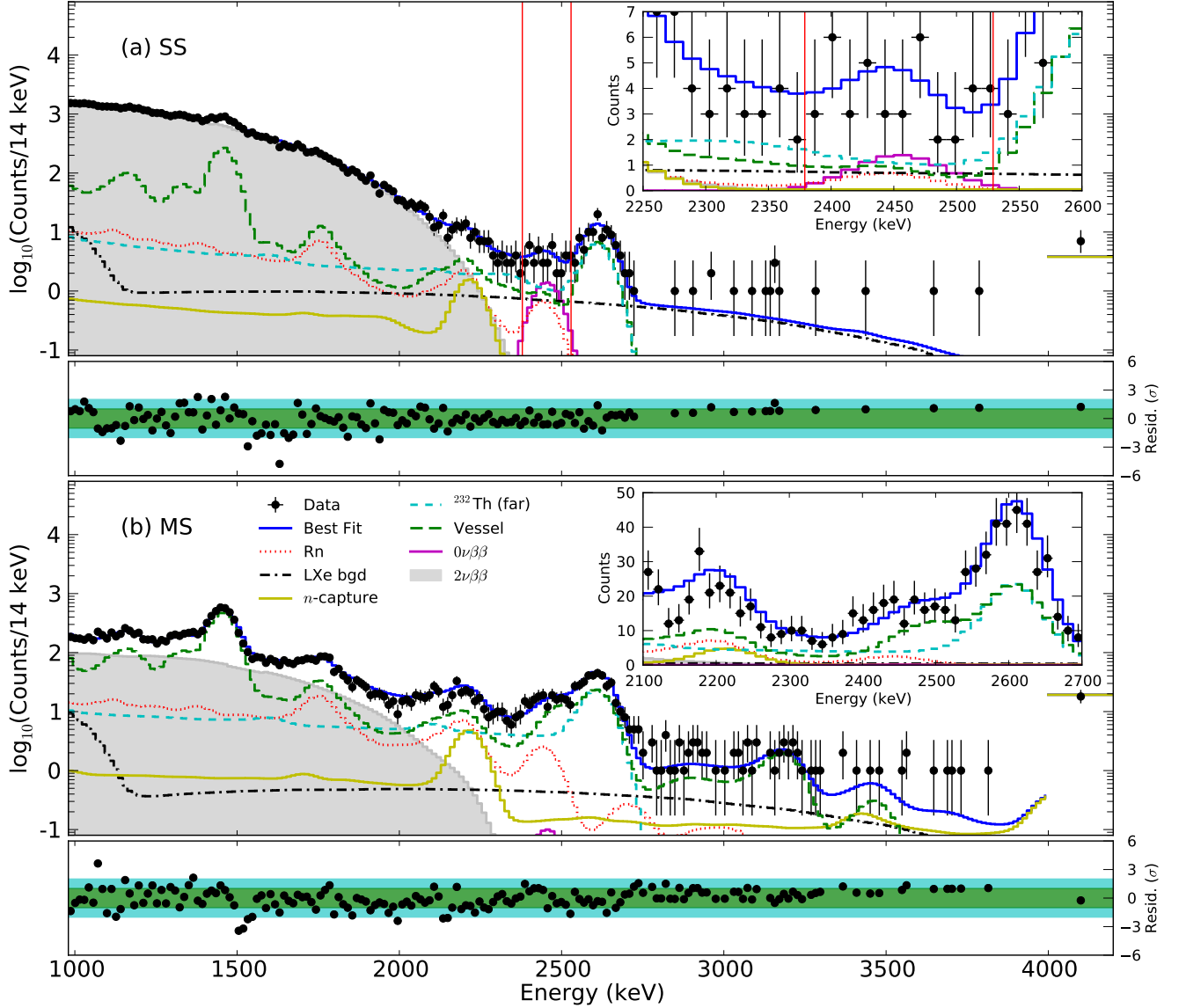


FIG. 4. (Color online) Fit results projected in energy for SS (a) and MS (b) events with a zoom-in (inset) around the ROI region: 2250–2600 keV (2100–2700 keV) for SS (MS). The bin size is 14 keV. Data points are shown in black and residuals between data and best fit normalized to the Poisson error are presented, ignoring bins with 0 events. The 7 (18) events between 4000 and 9800 keV in the SS (MS) spectrum have been collected into an overflow bin for presentation here. The vertical (red) lines in the SS spectra indicate the  $\pm 2\sigma$  ROI. The result of the simultaneous fit to the SD is not shown here.

SOURCES [23] software packages is used to generate neutrons, track and thermalize them. The resulting neutron capture rates are used as input to the Geant4-based [20] EXO-200 simulation package [9], with the respective  $n$ -capture  $\gamma$ -spectra produced based upon ENSDF information [24] for the given nuclides. The produced PDFs are used in fits to the low-background data. Good shape agreement is found between these PDFs and data coincident with muon-veto-panel events.

The fit to the low-background data minimizes the negative log-likelihood function constructed using a signal and background model composed of PDFs from simulation. A profile-likelihood (PL) scan is performed to

search for a  $0\nu\beta\beta$  signal.

The PDFs chosen for the low-background fit model are those used in [9] plus a “far-source”  $^{232}\text{Th}$  PDF and neutron-capture-related PDFs, including  $^{136}\text{Xe}$  neutron capture in the LXe,  $^1\text{H}$  neutron-capture in the HFE, and  $^{63}\text{Cu}$  and  $^{65}\text{Cu}$  neutron capture in Cu components (LXe vessel, inner and outer cryostats). The far-source  $^{232}\text{Th}$  PDF allows for background contributions from Th in materials far from the TPC, for example in the HFE and in the copper cryostat. (Remote  $^{238}\text{U}$  is included in the fit model via  $^{222}\text{Rn}$ , simulated in the air between the cryostat and Pb shield.) We combine the neutron-capture-related PDFs to form one PDF, allowing the rel-



Source	Error (%)
Background shape distortion	9.2
Background model	5.7
Energy resolution variation	1.5
Total	10.9

TABLE II. Estimation of systematic errors on the determination of background in the ROI arising from incorrect modeling of the background shape (Background shape distortion), incorrect or incomplete background model (Background model), and the residual variation of the energy resolution over time (Energy resolution variation, see e.g. Fig. 1).

ative rates of the component PDFs to float within 20% of their simulation-estimated values. The total rate of this summed PDF is allowed to float unconstrained.

We constrain the single-site fractions (SS/(SS+MS)) of all components to be within 9.6% of their value calculated from simulation. An additional 90% correlation between single-site fractions of  $\gamma$  components is introduced into the likelihood function, owing to the consistent behavior observed in these parameters in calibration studies (e.g. Fig. 3). The overall normalization is allowed to float within the estimated systematics errors (8.6%). The background-PDF amplitudes *within* the ROI are also allowed to vary within their estimated systematic error (10.9%). The  $\beta$ -scale is not allowed to float during the fit, but is manually profiled while performing the PL scan for  $0\nu\beta\beta$ .

The final step before performing the fit was the unmasking of live-time around the SS ROI. However, before unmasking the full data set, we investigated backgrounds associated with Xe feeds, irregular occurrences in which additional Xe gas is introduced into the purification circulation loop. (These Xe feeds occurred 10 times over the run period and are known to temporarily elevate, for example, Rn levels in the detector.) The live-time in the two-week periods following the 10 feed events were unmasked first to search for increased background levels in the ROI. No evidence for such an increase was found and the unmasking of the remaining live-time proceeded.

The results of the ML fit are presented in Fig. 4. The measured  $2\nu\beta\beta$  decay rate is consistent with [9]. From the best-fit model, the estimate of the background in the  $0\nu\beta\beta \pm 2\sigma$  ROI is  $31.1 \pm 1.8(\text{stat}) \pm 3.3(\text{sys})$  counts, or  $(1.7 \pm 0.2) \cdot 10^{-3} \text{ keV}^{-1} \text{ kg}^{-1} \text{ yr}^{-1}$  consistent with previous results [13]. The dominant backgrounds arise from  $^{232}\text{Th}$  (16.0 counts),  $^{238}\text{U}$  (8.1 counts) and  $^{137}\text{Xe}$  (7.0 counts). This amount of  $^{137}\text{Xe}$  is consistent with estimates from studies of the activation of  $^{136}\text{Xe}$  in muon-veto-tagged data. The total number of events seen in this region is 39. The best-fit value of  $0\nu\beta\beta$  counts is 9.9, consistent with the null hypothesis at  $1.2\sigma$  as calculated using toy Monte Carlo studies. The corresponding PL scan of this parameter is shown in Fig. 5.

A number of cross checks were performed on the re-

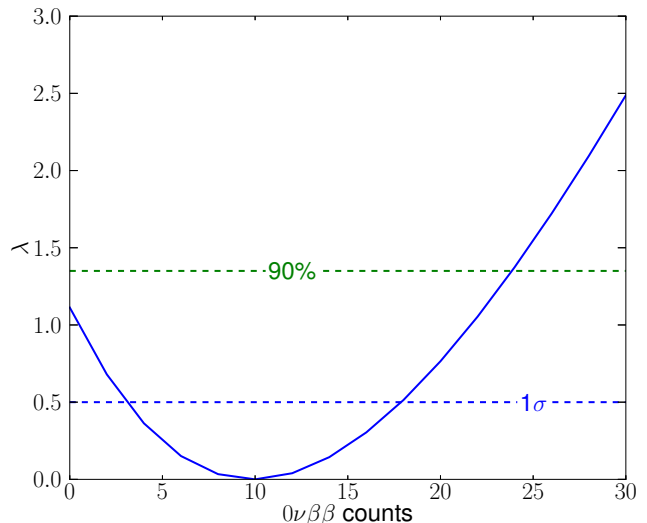


FIG. 5. (Color online) Profile likelihood,  $\lambda$ , for  $0\nu\beta\beta$  counts. The horizontal dashed lines represent the  $1\sigma$  and 90% confidence levels assuming the validity of Wilks' theorem [25], intersecting the profile curve at (3.1, 18) and 24  $0\nu\beta\beta$  counts, respectively. From toy Monte Carlo studies, the best-fit value is consistent with the null hypothesis at  $1.2\sigma$ .

sult. No event reconstruction anomalies were found after hand-scanning all events in the ROI. The time-between-events distribution of the ROI events is consistent with a constant-rate process and the spatial distributions of events do not reveal any nonuniformities. Additional backgrounds were considered that could contribute events to the ROI. In particular, we tested for  $^{110m}\text{Ag}$  and  $^{88}\text{Y}$  because of their possible association with the measurement in [12], and found that both produce a distinct high-multiplicity signature in EXO-200 ( $\sim 5\text{--}10\%$  SS/(SS+MS)). Separate fits including each of these PDFs contributed the following counts to the  $\pm 2\sigma$  ROI:  $N_{^{110m}\text{Ag}} = 0.04 \pm 0.02$  and  $N_{^{88}\text{Y}} = 0.02 \pm 0.01$ . Finally, we were able to exclude any significant effect on the ROI background from  $^{214}\text{Bi}$  external to the Pb shield, e.g. from  $^{238}\text{U}$  in the surrounding salt.

In summary, we report a 90% C.L. limit on the  $0\nu\beta\beta$  half-life of  $1.1 \cdot 10^{25}$  yr. With the nuclear matrix elements of [26–29] and phase space factor from [21], this corresponds to an upper limit on the Majorana neutrino mass of 190–450 meV. Using the three flavor fit of [30] we further use this range of effective mass limits to construct a constraint on the mass  $m_{\min}$  of the lightest neutrino mass eigenstate, assuming the most disadvantageous combination of CP phases. The EXO-200 limit corresponds to  $m_{\min} < 0.69\text{--}1.63$  eV, in case neutrinos are Majorana particles. The sensitivity of the experiment, defined as the median expected 90% CL half-life limit in the absence of a  $0\nu\beta\beta$  signal, is  $1.9 \cdot 10^{25}$  yr, among the best in the literature.

## ACKNOWLEDGMENTS

EXO-200 is supported by DOE and NSF in the United States, NSERC in Canada, SNF in Switzerland, NRF in Korea, RFBR (12-02-12145) in Russia and DFG Clus-

ter of Excellence “Universe” in Germany. EXO-200 data analysis and simulation uses resources of the National Energy Research Scientific Computing Center (NERSC), which is supported by the Office of Science of the U.S. Department of Energy under Contract No. DE-AC02-05CH11231. The collaboration gratefully acknowledges the WIPP for their hospitality.

- 
- [1] E. Majorana, *Nuovo Cimento*, **14**, 171 (1937), no. 4.
  - [2] G. Racah, *Nuovo Cimento*, **14**, 322 (1937), no. 7.
  - [3] V. Mourik, K. Zuo, S. M. Frolov, S. R. Plissard, E. P. A. M. Bakkers, and L. P. Kouwenhoven, *Science*, **336**, 1003 (2012).
  - [4] L. Camilleri, E. Lisi, and J. F. Wilkerson, *Annu. Rev. Nucl. Part. Sci.*, **58**, 343 (2008).
  - [5] R. N. Mohapatra and G. Senjanovic, *Phys. Rev. Lett.*, **44**, 912 (1980).
  - [6] M. Gell-Mann, P. Ramond, and R. Slansky, in *Supergravity*, edited by P. van Nieuwenhuizen and D. Freedman (North Holland Publishing Co, 1979) pp. 315–321, available arXiv:1306.4669.
  - [7] J. Schechter and J. Valle, *Phys. Rev. D*, **25**, 2951 (1982).
  - [8] A. Barabash, *Phys. Rev. C*, **81**, 035501 (2010).
  - [9] J. B. Albert *et al.* (EXO-200 Collaboration), *Phys. Rev. C*, **89**, 015502 (2014).
  - [10] P. Vogel, *J. Phys. G: Nucl. Part. Phys.*, **39**, 124002 (2012).
  - [11] M. Agostini *et al.* (GERDA Collaboration), *Phys. Rev. Lett.*, **111**, 122503 (2013).
  - [12] A. Gando *et al.* (KamLAND-Zen Collaboration), *Phys. Rev. Lett.*, **110**, 062502 (2013).
  - [13] M. Auger *et al.* (EXO-200 Collaboration), *Phys. Rev. Lett.*, **109**, 032505 (2012).
  - [14] H. Klapdor-Kleingrothaus and I. Krivosheina, *Mod. Phys. Lett. A*, **21**, 1547 (2006).
  - [15] M. Auger *et al.*, *JINST*, **7**, P05010 (2012).
  - [16] M. Redshaw, E. Wingfield, J. McDaniel, and E. G. Myers, *Phys. Rev. Lett.*, **98**, 053003 (2007).
  - [17] 3M HFE-7000, <http://www.3m.com>, (2014).
  - [18] E.-I. Esch, T. Bowles, A. Hime, A. Pichlmaier, R. Reifarth, *et al.*, *Nucl. Inst. & Meth. A*, **538**, 516 (2005).
  - [19] D. Leonard, P. Grinberg, P. Weber, E. Baussan, Z. Djuricic, *et al.*, *Nucl. Inst. & Meth. A*, **591**, 490 (2008).
  - [20] J. Allison, K. Amako, J. Apostolakis, *et al.*, *IEEE Trans. Nucl. Sci.*, **53**, 270 (2006), ISSN 0018-9499.
  - [21] J. Kotila and F. Iachello, *Phys. Rev. C*, **85**, 034316 (2012).
  - [22] G. Battistoni, F. Cerutti, A. Fassò, A. Ferrari, S. Muraro, J. Ranft, S. Roesler, and P. R. Sala, in *Hadronic Shower Simulation Workshop*, American Institute of Physics Conference Series, Vol. 896, edited by M. Albrow and R. Raja (2007) pp. 31–49; A. Ferrari, P. R. Sala, A. Fassò, and J. Ranft, *FLUKA: A multi-particle transport code (Program version 2005)*, Tech. Rep. CERN-2005-010, SLAC-R-773, INFN-TC-05-11 (CERN, 2005).
  - [23] W. B. Wilson, *SOURCES 4A : a code for calculating ( $\alpha, n$ ) spontaneous fission, and delayed neutron sources and spectra*, Tech. Rep. LA-13639-MS (Los Alamos National Laboratory, Los Alamos, NM, USA, 1999).
  - [24] M. Bhat, in *Nuclear Data for Science and Technology*, Research Reports in Physics, edited by S. Qaim (Springer Berlin Heidelberg, 1992) pp. 817–821, ISBN 978-3-642-63473-4, data extracted using the NNDC On-Line Data Service from the ENSDF database, file revised as of 1 June 2013.
  - [25] S. S. Wilks, *Ann. Math. Statist.*, **9**, 60 (1938); G. Cowan, *Statistical Data Analysis*, Oxford science publications (Clarendon Press, 1998).
  - [26] T. R. Rodriguez and G. Martínez-Pinedo, *Phys. Rev. Lett.*, **105**, 252503 (2010).
  - [27] J. Menéndez, A. Poves, E. Caurier, and F. Nowacki, *Nucl. Phys. A*, **818**, 139 (2009).
  - [28] J. Barea, J. Kotila, and F. Iachello, *Phys. Rev. C*, **87**, 014315 (2013).
  - [29] F. Šimkovic, V. Rodin, A. Faessler, and P. Vogel, *Phys. Rev. C*, **87**, 045501 (2013).
  - [30] D. V. Forero, M. Tórtola, and J. W. F. Valle, *Phys. Rev. D*, **86**, 073012 (2012); (2013), private communication.